Comparison of Mode I fracture toughness of an elastic and an elastoplastic methyl methacrylate polymer as measured by SENB and DCDC tests

Arnaud Coq, Julie Diani

Comparison of Mode I fracture toughness of an elastic and an elastoplastic methyl methacrylate polymer as measured by SENB and DCDC tests

A. Coq[a], J. Diani[a]

[a]*Laboratoire de Mécanique des Solides,UMR 7649, Ecole Polytechnique, 91128 Palaiseau, France*

Abstract

An elastic and an elastoplastic methyl methacrylate polymer, both in the glassy state, have been submitted to mode I fracture characterization with two different tests, the single edge notch bending (SENB) and the double cleavage drilled compression (DCDC) tests. The elastic material toughness was simply assessed by the linear elastic fracture mechanics analysis. For the elastoplastic material, the J-integral was computed when the strain fields were available. Moreover, numerical analyses were carried out using finite element simulations with a phase-field damage approach, providing comparison when the J-integral had been calculated and estimate otherwise, of the critical energy release rate. For each material, as well as for each test, the values of the critical energy release rate that have been estimated here, are in good agreement with the literature. More interestingly, for the same material, both tests provide with very different estimates of this material parameter, leaving engineers uncertain on which test to choose to asses the material toughness in crack opening mode.

Keywords: Fracture, Toughness, Polymer, Elastoplasticity, Phase-field approach

Email addresses: arnaud.coq@polytechnique.edu (A. Coq), julie.diani@polytechnique.edu (J. Diani)

1. Introduction

In an attempt to characterize the opening mode fracture of an elastoplastic polymer used for engineering applications, we faced the question of the test to apply among the numerous available, and of the similarity of the results considering various structural loadings. The literature is relatively well documented on fracture tests conducted on linear elastic brittle polymethyl methacrylate (PMMA). For the latter, the single edge notch bending (SENB) test seems dominant as Mode-I fracture characterization [1, 2, 3, 4, 5, 6, 7, 8, 9, 10]. However, the test is not carried out without practical difficulties and challenges of analysis. As for the experiment, the critical features are the pre-crack geometry and length. The initial macroscopic default may be a notch of V or U-shape, or a sharp crack. The raw experimental results depend on the notch angle [1, 4, 5] or how the pre-crack is made [11, 12, 13], and are very sensitive to the initial length of the notch or pre-crack [3, 13, 14]. For these reasons, it has been shown in [3] that determining the critical strain energy release rate, G_c, using a finite element framework, may be simpler than determining the critical stress intensity factor K_{Ic} with the linear elastic fracture mechanics analysis (LEFM) [1, 15].

SENB tests have been also applied to elastoplastic materials including polymers [16, 17], evidencing micro voids developing ahead of the crack. The fracture may still be fragile as fast and unstable when voids do not grow or coalesce, or may become ductile as slow and steady in the contrary case [16]. When slow ductile fracture happens, one may still characterize the critical energy release rate at crack initiation [18]. For monotonic loading, when the yielded zone near the crack tip is small compared to the sample dimensions and crack length, the energy release rate G may be estimated thanks to the J-integral [19] directly calculated from strain fields recorded on the exterior surface [17, 20].

The SENB test has been compared to other fracture tests. For instance, [21] reported comparable values of critical stress intensity factors for PMMA samples tested in compact tension (CT), double cantilever beam (DCB). [3] showed that it was possible to reproduce experimental SENB and single edge notch tension (SENT) fracture tests run on an elastoplastic PMMA considering the same cohesive zone softening model.

Other tests are possible to experimentally characterize Mode-I fracture of polymers. [22] submitted a PMMA to fracture tests with several tension geometries designed with holes where the tensile displacement is imposed

through pins. They showed satisfactory straight propagation for CT and tapered double cantilever beam specimens. However, it was recently shown [23] that boundary conditions are critical for such pin-loaded tests proving their analysis delicate.

In order to extend the comparison, we have submitted an elastic and an elastoplastic methyl methacrylate polymer to SENB and double cleavage drilled compression (DCDC) mode I fracture characterizations. During the DCDC test, cracks initiated at both poles of a hole drilled in the center of a slender parallelepiped, are submitted to opening mode when the specimen is in uniaxial compression. The test has been originally introduced for glasses and successfully extended to polymers [24, 25, 26, 27, 28]. However, the resulting critical energy release rate has been scarcely compared to values obtained with other tests. In the domain of linear elastic fracture mechanics, the stress intensity factors K_{Ic} recorded by SENB and DCDC tests have been compared twice. In the case of a PMMA, [29] reported a SENB K_{Ic} value 15% higher than the DCDC K_{Ic} value. Still for a PMMA, [30] reported a different result in terms of a DCDC K_{Ic} value twice larger than the value obtained by a four-point bending test. Albeit focusing on brittle materials only, yet no consensus has been reached on the comparative outcomes of DCDC and SENB tests.

Therefore, both materials have been submitted to SENB and DCDC tests considering pre-notches made with a diamond wire and pre-cracks made with a razor blade. For the elastic PMMA, the critical energy release rate values are estimated using the LEFM for both tests. For the elastoplastic specimens submitted to 3-point bending, the strain field obtained by digital image correlation allowed a direct calculation of the J-integral [19]. Unfortunately, the strain field was not accessible during the DCDC test due to the application of lubricant between the sample and a required none-buckling system added on both sides of the sample. However, both tests have been reproduced by finite element analysis using the phase-field damage approach [31], providing with reliable estimates of the critical energy release G_{I_c} at fracture initiation. The results, which individually compare well with the literature, show that, for both materials, the DCDC critical fracture energy release rate values stand significantly below the single edge notch bending test values.

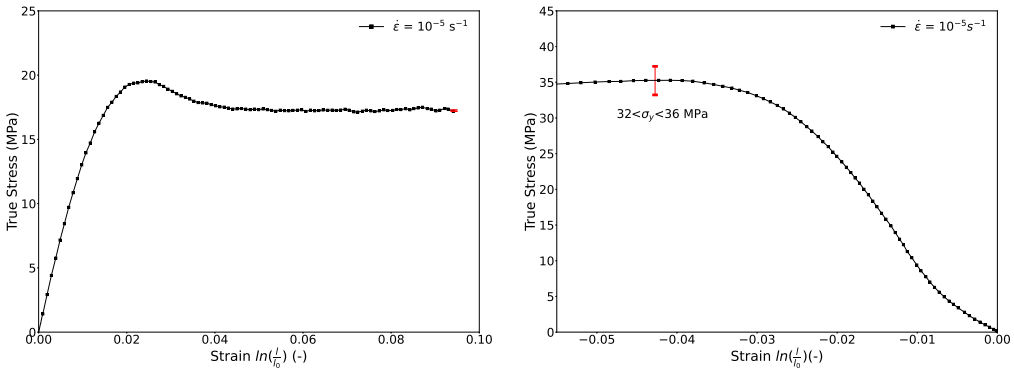

(a) (b)

Figure 1: W47 material uniaxial stress-strain responses at low strain rate (10^{-5} s^{-1}) - (a) Uniaxial tension (b) Uniaxial compression.

2. Materials and Experiments

2.1. Materials

Two methyl methacrylate polymers have been studied. The first one is a commercial cast PMMA supplied as parallelepiped of dimensions 20 x 20 x 80 mm^3 for SENB tests and 12 x 12 x 50 mm^3 for DCDC tests. It was chosen for its isotropic linear elastic behavior, its excellent transparency favoring crack observations, and the fact that the literature provides with solid comparisons for PMMA. The second material, labeled W47, has been supplied by Bostik (ARKEMA). It is a thermoplastic methyl methacrylate adhesive, which polymerizes at room temperature. The polymer was received in ready-to-use cartridges and was injected in Teflon molds with a twin-screw glue gun to obtain samples with the desired geometries. The dark color polymer did not have the transparency benefit of the PMMA.

Due to the sample geometry, the PMMA was submitted to uniaxial compression only. A linear elastic behavior characterized by a Young Modulus of 1710 MPa and a Poisson ratio of 0.40 was recorded at the low strain rate 10^{-5} s^{-1}. Material W47 was submitted to uniaxial compression and uniaxial tension at the same constant strain rate. This material showed an elastoplastic behavior with similar elastic characteristics, as $E = 1470$ MPa and $\nu = 0.42$ in tension and $E = 1400$ MPa and $\nu = 0.40$ in compression and different yield stresses, as $\sigma_y = 20$ MPa in tension and $\sigma_y = 34$ MPa in compression (Figure 1).

2.2. SENB tests

This section details the notch or pre-crack making, test parameters, and result analysis for the SENB test.

2.2.1. SENB samples

The length L × width w × thickness t of the samples are 80 × 20 × 20 mm^3 for PMMA and 80 × 17 ± 0.1 × 7.6 ± 0.7 mm^3 for W47.

As previously mentioned, the notch or pre-crack technique has a significant impact on the experimental results. For each material, two techniques were performed. First, a diamond wire was used to create a notch of either half or a quarter of the specimen width (Figure 2a). Second, for the specimens with the smaller notches, a flat razor blade was inserted in the pre-notch and tapped to initiate a pre-crack using a specifically designed setup 2c). Note that the final pre-crack length obtained for MMA samples was quite variable while for the PMMA samples, good repeatability was achieved, with an average length of 0.56×w. The literature mentions the significant impact of the initial pre-crack length on this test. Consequently, each pre-crack and pre-notch was measured under an optical microscope, and samples with a pre-notch or pre-crack deviating from the vertical alignment by an angle larger than 2° were discarded.

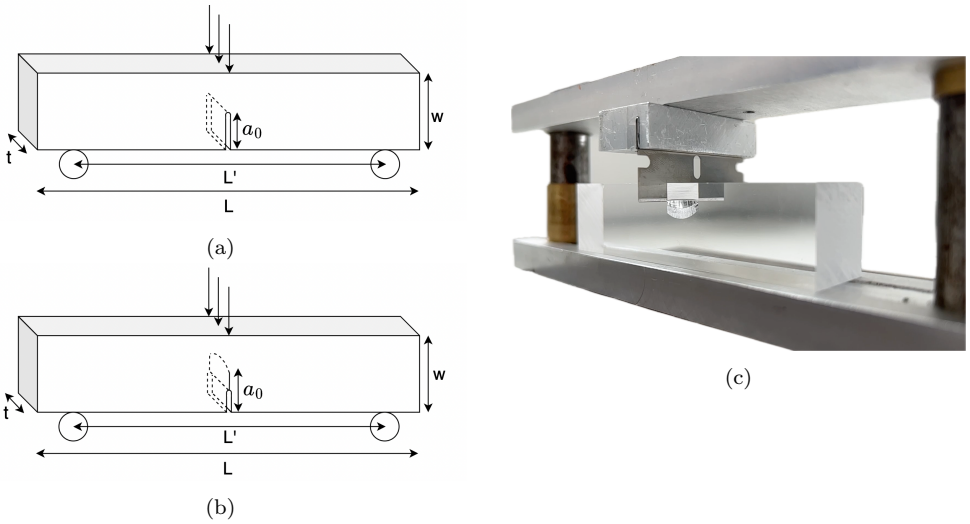

Figure 2: Illustration of SENB (a) pre-notched and (b) pre-cracked samples. (c) shows a pre-crack obtained by tapping a razor blade inserted in the notch.

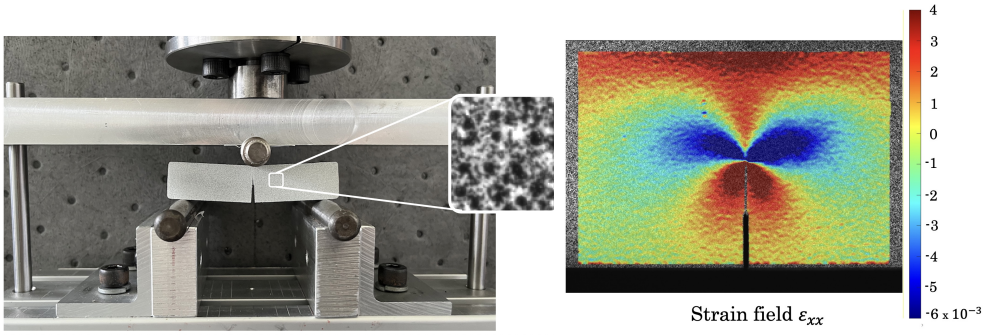

(a) (b)

Figure 3: (a) SENB experimental setup (b) W47 resulting strain field characterized by digital image correlation for a pre-cracked sample

2.2.2. SENB setup

The SENB tests (Figure 3a) were conducted on a Instron 5967 testing machine at a constant crosshead speed of 0.1 mm/min. A JAI SP-20000 camera (20M pixels) equipped with a 1.0 magnification telecentric lens and a resolution of 6.4 μm/pixel was set to follow the crack propagation and estimate the strain field on the exterior face.

Due to its natural transparency, tracking the PMMA crack length was easily performed using a mere digital ruler. Given the darker color of W47, the crack progression could be monitored on the external surface only. Additionally, a speckle pattern has been applied on the surface of the samples to characterize the strain field using 2D digital image correlation (Figure 3b). We used the open-source software `Ncorr` [32], which is based on a local approach, and has been proven to provide with good performance compared to commercial software [33]. Correlation parameters, such as subset size and window size for strain field calculations, were chosen to balance spatial resolution and noise, aiming for accurate strain and displacement values in high-gradient areas. A correlation step of 2 was selected for precise measurements without unnecessarily extending computation duration. The selected subset radius is set to 15 px and a strain window radius of 7 px. This leads to an estimate of the size of virtual strain gauge to 56 px, or 0.33 mm.

2.2.3. SENB experimental results

Firstly, we report the PMMA results. We have plotted the resulting force with respect to the applied displacement in Figures 4a and 5a. Both types of

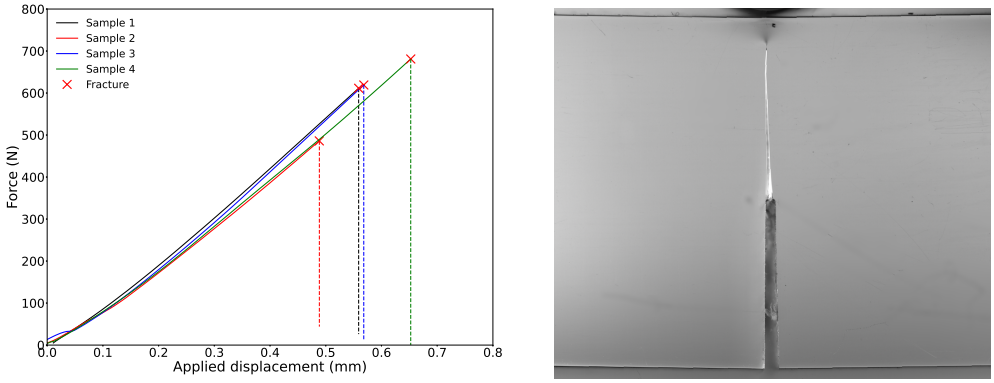

(a) (b)

Figure 4: (a) SENB fracture test resulting force with respect to applied displacement as catastrophic cracks grow instantaneously for pre-notched PMMA samples, illustrated in (b).

samples show linear responses until the cracks propagate with excellent experimental reproducibility. For pre-notched samples, instantaneous complete failures prevent from following crack growths. For pre-cracked samples, crack initiations occur at a significantly lower macroscopic force, and the much slower crack propagations can be followed (Figure 5b). These differences between pre-notched and pre-cracked samples comply with the literature [11].

The critical energy release rate G_c at crack initiation has been evaluated using the area method Eq. (A1.2) in [34] for pre-notched samples and the area difference δA during an increase of the crack length of δa, as $G_c = \frac{\delta A}{t \delta a}$ for the pre-cracked samples. Average values were estimated over four samples at 1.6 kJ/m^2 with a standard deviation of 0.4. for the pre-notched samples, and 0.42 kJ/m^2 with a standard deviation of 0.05 for the pre-cracked samples. The values reported in the literature for commercial pre-cracked PMMA and obtained with different tests (wedge splitting, central notch, tensile test, SENB) [35, 36, 37, 38, 39], ranges between 0.3 and 0.6 kJ/m^2, which is comparable. The higher value of G_c obtained for pre-notched samples, is referred as an 'apparent' fracture toughness in several studies [40, 41, 42]. This value is not merely a material parameter anymore and the use of linear fracture mechanics is debatable.

Secondly, we discuss the results for W47. Due to some thickness variability among our lab-made samples, the resulting force has been normalized by this geometrical parameter in Figures 6a and 7a. The tests on pre-cracked

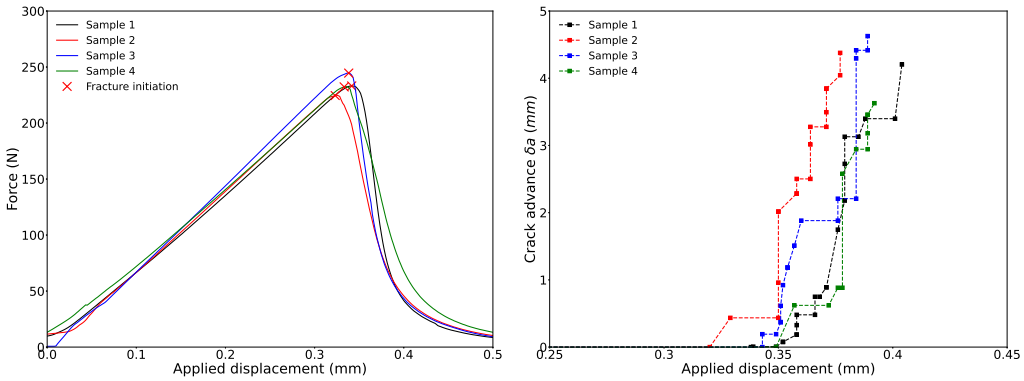

(a) (b)

Figure 5: SENB fracture test (a) resulting force and (b) crack growth with respect to applied displacement for pre-cracked PMMA samples.

samples have shown a significant variability on the initial slope, the maximum force reached, and the applied displacement at crack initiation. This is explained by the variability in the geometrical factor, a_0/w, revealing the structural dependence of this test already mentioned in [11, 43].

The elastoplastic behavior of W47 is not only witnessed in the shape of the structure responses in Figures 6a and 7a. For both pre-notched and pre-cracked samples, the cracks propagate by steps and plateaus are clearly visible in Figures 6b and 7b. Independently of the initial damage, the post-mortem analyses reveal crack surfaces that are rough showing many cavities, which is an obvious sign of plasticity developing at the crack tip.

Due to the elastoplastic behavior of this material, the use of LEFM analysis may carry significant errors. However , under monotonic loading and small-scale yielding, one may use the J-integral [19],

$$J = \int_C W dy + \sigma_{ij}\, n_j\, \frac{\partial \underline{u}}{\partial x}\, dS \tag{1}$$

to compute the energy release rate and extract G_c at crack initiation. The extension of J to elastoplastic materials, such as polymers and composites has been proven successful in some cases [44, 17, 45]. Thanks to the strain field obtained by digital image correlation (Figure 3), the integral J has been computed on a 1D path, for which the material behavior is well described by the elastic constants $E = 1400$ MPa and $\nu = 0.4$ (details are given in Appendix A). Based on three samples, G_c was consequently determined at

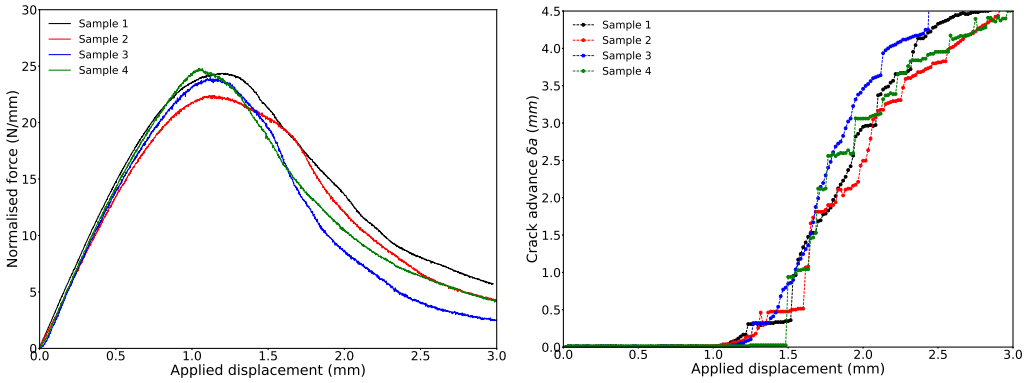

(a) (b)

Figure 6: W47 SENB fracture test (a) resulting force normalized by the sample thickness t and (b) crack growth, with respect to applied displacement for pre-notched samples.

an average of 3.38 kJ/m^2 with a standard deviation of 0.48 for pre-notched samples and at an average value of 2.866 kJ/m^2 with a standard deviation of 0.16 for pre-cracked ones. These values are relevant only if the energy dissipated by plasticity is relatively negligible, which remains to be validated by a finite element analysis for instance.

2.3. DCDC tests

The DCDC test consists in a long prism, with a hole in the middle and vertical cracks at the poles of the hole, submitted to a compressive loading on its top face. Like for the SENB test, this section presents the making of the initial cracks, the test parameters and a first test analysis.

2.3.1. DCDC sample preparation and loading conditions

The PMMA parallelepiped samples have the dimensions $w \times t \times L$ equal to $12 \times 12 \times 50$ mm^3. A hole of radius $R = 1.5$ mm was drilled in the middle. Note that the impact of the geometry and more specifically of the sample thickness has been studied in [26]. The authors' analysis covered plane-strain, plane-stress and 3D finite element simulations. They showed that the changes in K_{Ic} was about 10% only when varying the sample thickness from 3 mm to 11 mm for samples of 50 mm length and 12 mm width. In order to initiate cracks at the poles of the hole, several options have been described in the literature. We tried to submit the specimens to a cyclic compression increasing the maximum load gradually until pre-cracks appear

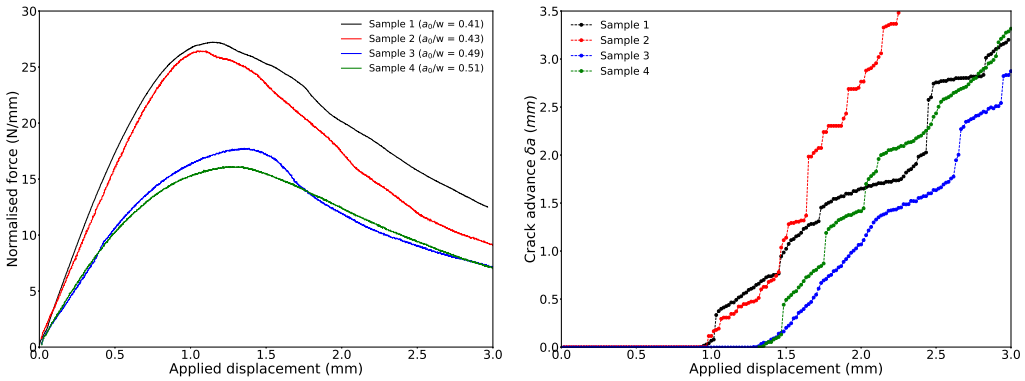

(a) (b)

Figure 7: W47 SENB fracture test (a) resulting force normalized by the sample thickness t and (b) crack growth, with respect to applied displacement for pre-cracked samples.

[26]. This technique resulted in the localization of significant plastic strain before any initiation (Figure 8a). When using a razor blade, [11] recommend to tap the blade rather than to insert it slowly, in order to limit the residual stresses at the crack tip. Therefore, a specific assembly was set, consisting in a triangular pipe-cutting razor blade (RS PRO 15 mm) mounted on a metal holder positioned above the sample hole, as illustrated in Figure 8. The blade was tapped by dropping a 300 g mass from a 200 mm height on the metal holder.

W47 samples were casted in a mold designed to eliminate the hole drilling step. After polishing the final dimensions of the samples are $L = 47 \pm 1$ mm, $w = 11.6 \pm 0.1$ mm, and $t = 4.2 \pm 0.2$ mm. For this material, the razor blade technique was generating significant plastic strain at the poles of the hole. Therefore, a diamond wire of 0.3 mm diameter was used to create pre-cuts into the specimens resulting in pre-notched samples. Unfortunately, the same technique could not be applied to the PMMA due to its high hardness. Consequently, only pre-cracked PMMA samples and pre-notched W47 samples were at our disposal to carry out DCDC tests. The compressive displacement has been applied on the top surface of the sample at a constant speed of 0.5 μm/s, equivalent to a strain rate of 10^{-5} s^{-1}.

2.3.2. DCDC experimental results

For the PMMA, the macroscopic stress-strain response shows a nearly linear loading slope followed by a rapid drop in stress when the crack initiates,

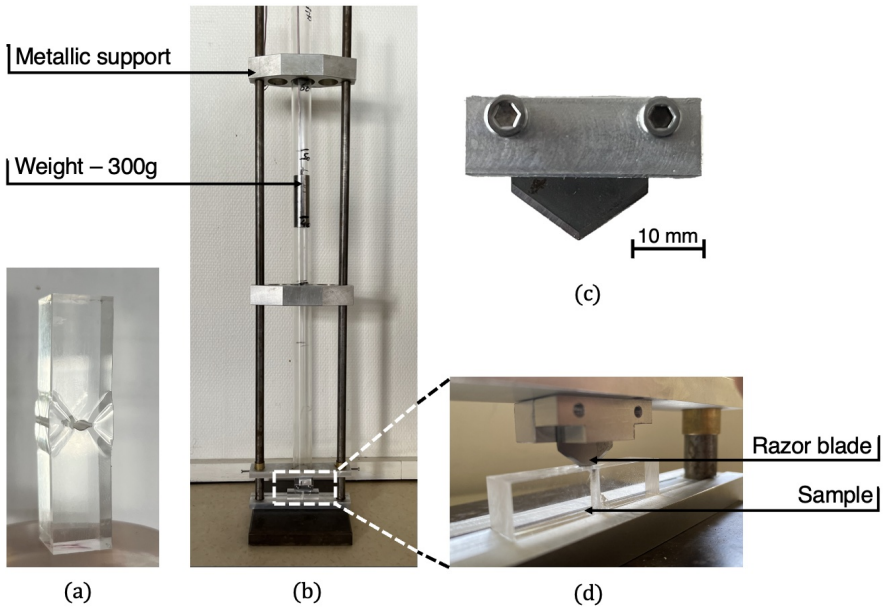

Figure 8: PMMA DCDC sample preparation (a) Trial to create pre-cracks by cyclic compressive loading, the material shows significant plastic strain before crack initiation at the poles of the hole (b) Setup designed for tapping a triangular razor blade (c) positioned on the sample as shown in (d).

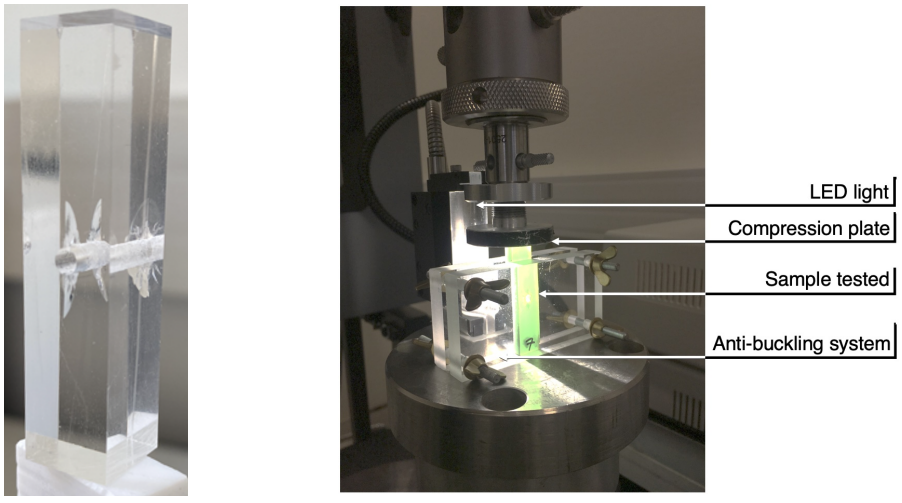

Figure 9: (a) PMMA DCDC sample after pre-cracking method and (b) Experimental set-up for W47 samples preventing specimen buckling.

which is marked by a red cross in Figure 10a. Figure 10b illustrates the crack progression with respect to the applied strain. It starts at approximately 3.6%, and evolves very rapidly, reaching a length of more than 10 mm after an additional 0.2% strain only. Nonetheless, the crack propagation is rather stable, like it has been observed in other studies [26, 30].

It has been mentioned previously that significant plasticity appeared around the hole when a cyclic loading was applied on a sample without pre-damage around the hole. However, after the cracks progagated, the postmortem analysis of the specimens did not present any residual strain, allowing us to apply the LEFM analysis with confidence. In such a context, the critical energy release rate may be simply calculated through the expressions of the stress intensity factor that have been proposed in the literature [46, 47, 48, 26, 25, 49, 50]. Using the work from [50], which includes our geometry and crack sizes ($0.4 \leq \frac{a}{R} \leq \frac{w}{R}$ and $2 \leq \frac{w}{R} \leq 6$), we obtained an average critical energy release rate of 0.12 kJ/m^2 with a standard deviation of 0.01, which is of the order of values reported by [26]. The latter characterized the stress intensity factor K_{Ic} between 0.6 and 0.75 MPa.m$^{1/2}$ for a PMMA presenting a Young modulus of 3100 MPa and a Poisson ratio of 0.4, which is equivalent to values of $G_c(= \frac{K_{Ic}^2}{E(1-\nu^2)})$ ranging between 0.14 and 0.22 kJ/m^2 for plane strain modeling. Finally, the average value of 0.12 kJ/m^2 falls also in the range of values reported by studies focused on other tests such as wedge cleavage [26, 38, 51].

The DCDC results for W47 have been reported in a previous contribution [28] and therefore are not detailed here. The macroscopic stress-strain curves showed a plasticity plateau during which the crack initiates and propagates. The crack advance is smooth and does not show some steps as for the SENB tests. The critical energy release rate cannot be determined simply since no analytical expressions are available in the case of plastic materials, and the none-buckling system prevented to measure the local strain fields and calculate the J-integral. Therefore, it will be estimated later using finite elements simulations including a damage model as presented in the next section.

Table 1 lists the critical energy release rate values that have been obtained so far with relatively simple analyses of the experiments. Focusing on the pre-cracked PMMA samples, for which one can already make a direct comparison. As a reminder values obtained for each SENB and DCDC test are in good agreement with the literature. When comparing the values between both

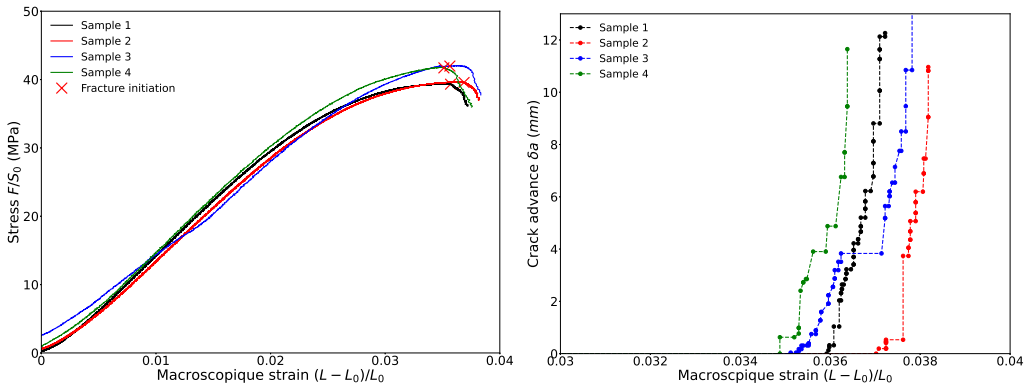

(a) (b)

Figure 10: PMMA DCDC fracture tests (a) Macroscopic stress-strain responses, the red cross indicates the crack initiation and (b) crack growth, with respect to applied macroscopic compressive strain.

	PMMA	MMA
SENB Pre-notched	1.6	3.38
SENB Pre-cracked	0.42	2.86
DCDC Pre-notched	-	-
DCDC Pre-cracked	0.12	-

Table 1: Experimental estimates of the critical energy release rate values in kJ/m^2.

tests, there is a significant discrepancy, with a ratio of three between the SENB value and the DCDC value. While the trend is in agreement with the results reported by [29], the order of magnitude of the discrepancy is significantly higher here.

The next section presents the damage-based finite element framework that has been applied to estimate the critical energy release rate for both SENB and DCDC tests, for elastic perfectly plastic W47 material.

3. Finite element damage-based fracture modeling for the elastic perfectly plastic material

3.1. Phase-field damage approach

The phase-field damage approach was initially introduced by [31] who revisited the Griffith criterion by a variational approach. It has been immediately followed by the regularized formulation of [52] proposing an ap-

proximation of the energy to minimize, within the Γ-convergence. This regularized formulation has since became standard for it eases the numerical computations. Then, the original formulation defined in the context of linear elasticity, has been extended to elastoplasticity in several studies, both in small strain [53, 54, 55, 56, 57] and large strain [58, 59]. The minimization problem is formulated as follows,

$$(\underline{u}^*, \underline{\underline{\epsilon_p}}^*, d^*)_\ell = \underset{\substack{\underline{u}\in\mathcal{U}_{ad},\ \underline{\underline{\dot{\epsilon}_p}}\in\mathcal{G},\\ \dot{d}\geq 0}}{\arg\min} \ \mathcal{E}_\ell(\underline{u}, \underline{\underline{\epsilon_p}}, d) \tag{2}$$

where $\mathcal{G}$ is the set of incompressible plastic strain rates, $\underline{\underline{\epsilon_p}}$ the plastic strain and d a regularized scalar field ranging in $[0, 1]$, which represents the damage state of the material, with 0 and 1 the intact and fully damaged states respectively. The material is considered as elastic perfectly plastic, satisfying to the von Mises criterion, $\sqrt{\frac{3}{2}\underline{\underline{s}} : \underline{\underline{s}}} \leq \sigma_y$, where $\underline{\underline{s}} = \underline{\underline{\sigma}} - \frac{tr(\underline{\underline{\sigma}})}{3}\underline{\underline{1}}$ is the deviatoric part of the Cauchy stress tensor. The sum of the elastic and plastic strains define the total strain, $\underline{\underline{\epsilon}}$, and the stress-strain relationship classically writes as, $\underline{\underline{\sigma}} = \mathbb{C}(\underline{\underline{\epsilon}} - \underline{\underline{\epsilon_p}})$. Therefore, following the AT1 model [60], the total energy of the system may be expressed as,

$$\begin{aligned} \mathcal{E}_\ell\left(\underline{u}, \underline{\underline{\epsilon_p}}, d\right) &= \int_\Omega W^{el} + W^{plas} + W^{frac}\, d\Omega \\ &= \int_\Omega \frac{1}{2}\left(\underline{\underline{\epsilon}} - \underline{\underline{\epsilon_p}}\right) : (1-d)^2\,\mathbb{C} : \left(\underline{\underline{\epsilon}} - \underline{\underline{\epsilon_p}}\right)\, d\Omega \\ &+ \int_\Omega b\,(d)\sqrt{\frac{2}{3}}\sigma_y \overline{p}\, d\Omega + \int_\Omega \frac{3G_c}{8}\left(\frac{d}{\ell} + \ell\,|\nabla d|^2\right)\, d\Omega, \end{aligned} \tag{3}$$

where $\overline{p} = \int_0^t |\dot{\epsilon}_p|\, \mathrm{d}\tau$ is the accumulated plasticity. The degradation function $b(d)$, is often defined as $(1-d)^2$ in order to decouple plasticity from damage [56, 54]. However, other options are possible [61], and three cases will be tested here as 1, $(1-d)$ and $(1-d)^2$. Finally, ℓ is a small regularization parameter, strictly positive, defining the width of the damaged band representing the cracks.

The SENB test is expected to show limited plasticity while the DCDC test is mostly a compression test. Therefore, we had chosen to run simulations for a von Mises material assuming the yield stress at 34 MPa, thus benefiting from the fact that the von Mises plastic model limits the numerical difficulties. However, when reading Figure 1, one may want to explore the

impact of considering a Drucker-Prager plasticity criterion, which is shown in Appendix Appendix B.

3.2. Numerical aspects

The minimization of $\mathcal{E}_\ell$ is achieved at each time step t^i by,

1. Firstly, finding the optimal kinematically admissible displacement $\underline{u}^i$ and the admissible plastic strain $\underline{\underline{\epsilon_p}}^i$, while keeping the damage variable d^{i-1} constant. The accumulated plasticity is updated as $\overline{p}_i = \overline{p}_{i-1} + \|\underline{\underline{\epsilon_p}}^i - \underline{\underline{\epsilon_p}}^{i-1}\|$, where the norm $\|\underline{\underline{a}}\| = \sqrt{\underline{\underline{a}} : \underline{\underline{a}}}$.
2. Secondly, minimizing the damage field d while keeping $\underline{u}^i$ and $\underline{\underline{\epsilon_p}}^i$ constants, with the constraint that $\dot{d} \geq 0$.

This process is repeated iteratively until convergence is achieved. Note that, despite running 2D simulations, the strain and stress tensors are written in three dimensions to consider plane stress or plane strain assumptions. The plastic incompressibility condition $tr\, \underline{\underline{\dot{\epsilon}_p}} = 0$, is enforced during the minimization by penalization.

The finite element implementation was made on open source computing platform FEniCS [62]. The displacement field $\underline{u}$ was computed by energy minimization with the direct solver `MUMPS`, the plastic strain field $\underline{\underline{\epsilon_p}}$ thanks to the nonlinear solver `SNES PETSc`, and finally, the damage field $\overline{d}$ thanks to the library `PETSc TAO`.

Meshes were generated with open source gmsh [63] with controlled refinement down to $\ell/5$, in the crack vicinity as illustrated in Figure 11. On one hand, for pre-notched samples, the crack tip is modeled by a 3 mm wide U-shaped notch. On the other hand, for pre-cracked samples, the mesh reproduces the 3 mm wide U-shape pre-notch for a height equal to one quarter of the sample height, and a sharp pre-crack making an angle of 0.2° only, is added starting from the top of the U-notch and reaching the same length as measured experimentally.

An initial full damage, $d = 1$, has been applied at the crack tip of the pre-cracked sample. This condition avoids unrealistic delays for the crack initiation [28]. However, in the case of the pre-notched sample, this condition is unnecessary. Dirichlet boundary conditions are applied on the top face for the DCDC test, and at the upper support, realistically represented by a band of 1 mm width, for the SENB test.

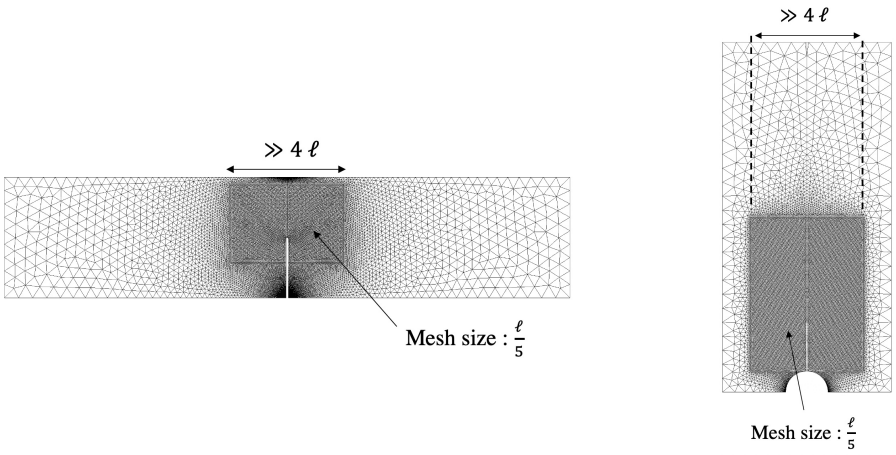

(a) (b)

Figure 11: Mesh refinement for the (a) SENB and (b) DCDC test.

4. Results

The experimental tests run on material W47 are now reproduced with the phase-field approach, accounting for the elastic perfectly plastic behavior of the material, in order to estimate the material critical energy release rate G_c without neglecting the plasticity dissipation. In order to validate the material inputs, we compare the numerical solution to the experimental macroscopic stress-strain response and strain fields obtained by image correlation before crack initiation. Then, we focus on the crack initiation to determine G_c.

4.1. Fracture toughness for W47 pre-notched SENB samples

Simulations are run within the plane strain assumption due to the sample thickness, and with material parameters obtained in compression, $E = 1400$ MPa, $\nu = 0.4$, and $\sigma_y = 34$ MPa. Experimental and numerical strain fields are satisfactorily compared in Figure 12, for an applied displacement of 0.8 mm that is close to crack initiation (Figure 6). Figure 12 presents local strains ϵ_{xx} and ϵ_{yy} using the same scales for the experimental and the numerical fields. Satisfactory comparisons of the local strains go with a perfect reproduction of the initial macroscopic response displayed in Figure 13. Both results support the material behavior parameters applied in the numerical simulations.

Now focusing on the fracture part of the test, a value of $G_c = 3.5$ kJ/m^2 is chosen driven by the experimental results (Table 1). The function $b(d)$ in

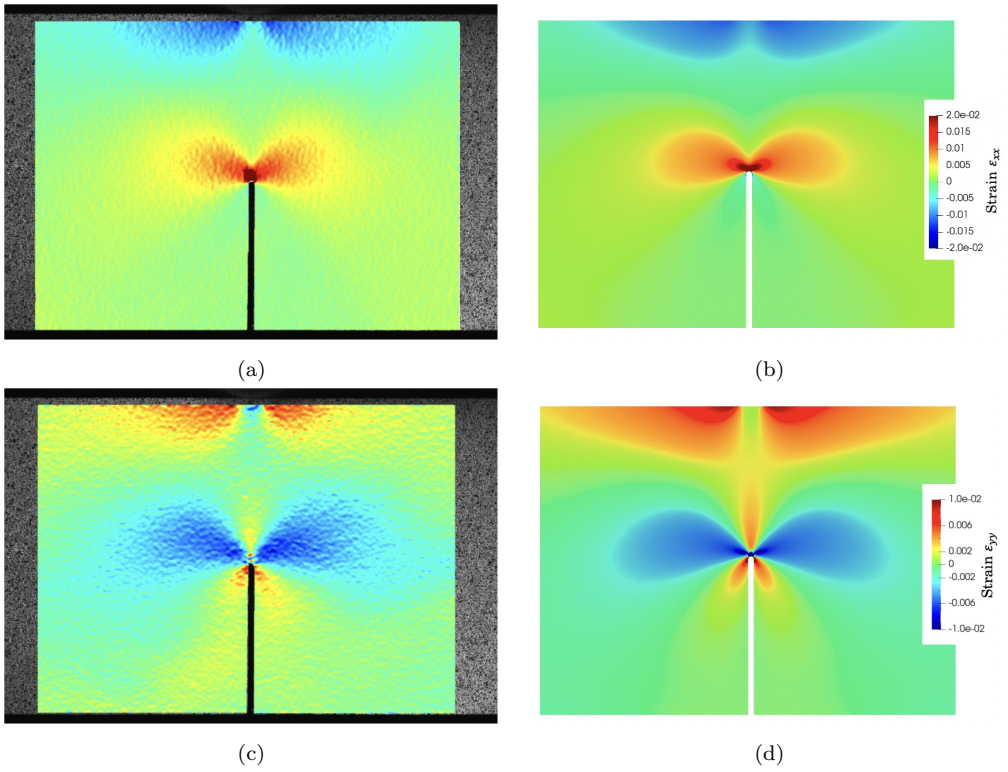

(a) (b)

(c) (d)

Figure 12: Comparison of the experimental (left) and numerical (right) strain fields for W47 SENB pre-notched samples at a macroscopic compressive displacement of 0.8 mm. x stands for the horizontal strain and y for the vertical one.

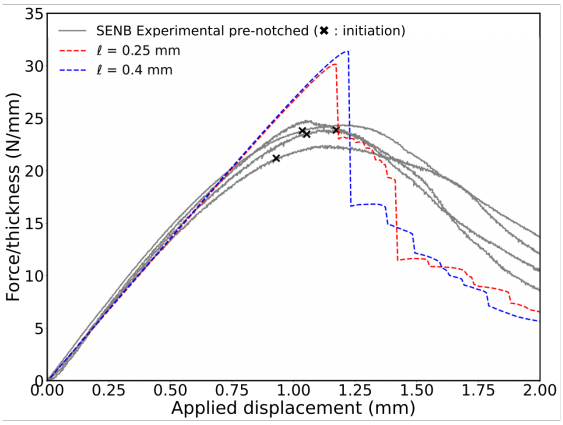

Figure 13: Phase-field modeling of the fracture of W47 pre-notched samples for $G_c = 3.5$ kJ/m^2.

Eq. (3) is first classically set to $(1-d)^2$. The last model parameter, ℓ, is set to reproduce the strain at break of an undamaged sample submitted to a simple uniaxial tensile test as proposed in [64]. Doing that, satisfactory strain at break values were obtained when ℓ was varied between 0.25 and 0.40 mm. The numerical results for the fracture are displayed in Figure 13. The fracture onset is delayed as ℓ decreases. At crack initiation, while the stress is overestimated, the strain is correct for $\ell = 0.25$ mm, which is in favor of a critical energy release rate in the vicinity of 3.5 kJ/m^2 as estimated with the J-integral. This result is confirmed when analyzing the amount of plastic dissipation upon loading. It is limited to 5% of the total energy at crack initiation, revealing that plasticity could be neglected as it was done when calculating the J-integral. Finally, the negligible plasticity is logical when looking at its localization limited to the crack tip only (Figure 14).

As for the crack propagation, one notes that the model predicts a sudden drop in the stress that is not representative of the experiments. The crack propagates by steps, which has been reported already in the context of plane strain [54]. This result does not match the experimental reality and therefore it is preferable to limit our analysis to the crack initiation, recognizing that future work should analyze the crack propagation.

Finally, when changing the coupling between damage and plasticity, replacing $b(d) = (1-d)^2$ by $b(d) = 1$ or $b(d) = (1-d)$, behavior at crack initiation differs. For $b(d) = 1$, fracture initiation is clearly delayed compared to the one observed using $b(d) = (1-d)^2$, the macroscopic response of

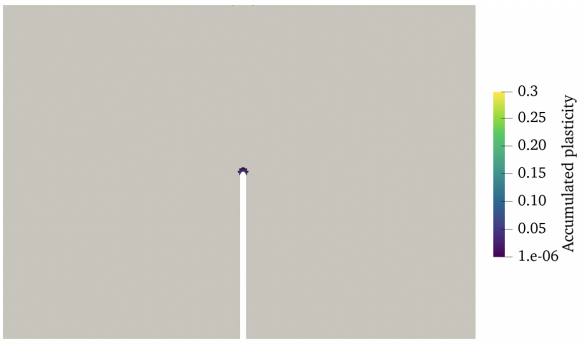

Figure 14: Illustration of accumulated plasticity $\overline{p}$ for W47 pre-notched sample at an applied macroscopic displacement of 0.8mm. Values under 0.001 (or 0.1 %) are displayed in gray.

the structure being the one of an elastic/fragile material. For $b(d) = (1-d)$, the plasticity at the crack tip is slightly reduced and the macroscopic displacement at crack initiation is slightly increased. Finally, it is worth noting that the case $b(d) = (1-d)^2$ was the easiest one in terms of numerical convergence and that we could not follow the propagation for the two other ones.

4.2. Fracture toughness for W47 pre-cracked SENB samples

We adopt the same plane strain assumptions and the same material parameters as in the previous section. Following the same path, the experimental and numerical strain fields are compared for 0.8 mm of macroscopic displacement. Satisfactory comparison of the local strain fields are reported in Figure 15 where the same scales are used again for the experimental and the numerical fields. Moreover, the initial macroscopic response is also well reproduced (Figure 16).

As in the case of pre-notched samples, we chose a value for G_c close to the experimental results reported in Table 1. Then, for $G_c = 3.0$ kJ/m^2 and $b(d) = 1 - d^2$ in Eq. (3), the range of suitable values for ℓ has been determined by matching the numerical strain at break of an undamaged sample in uniaxial tension to the experimental one. Satisfactory results were obtained for $\ell \in [0.15, 0.35]$.

The numerical results for the fracture SENB test are displayed in Figure 16 for three values of ℓ. This time, the fracture onset is delayed as ℓ decreases. The strain at fracture initiation is well reproduced for the larger values of

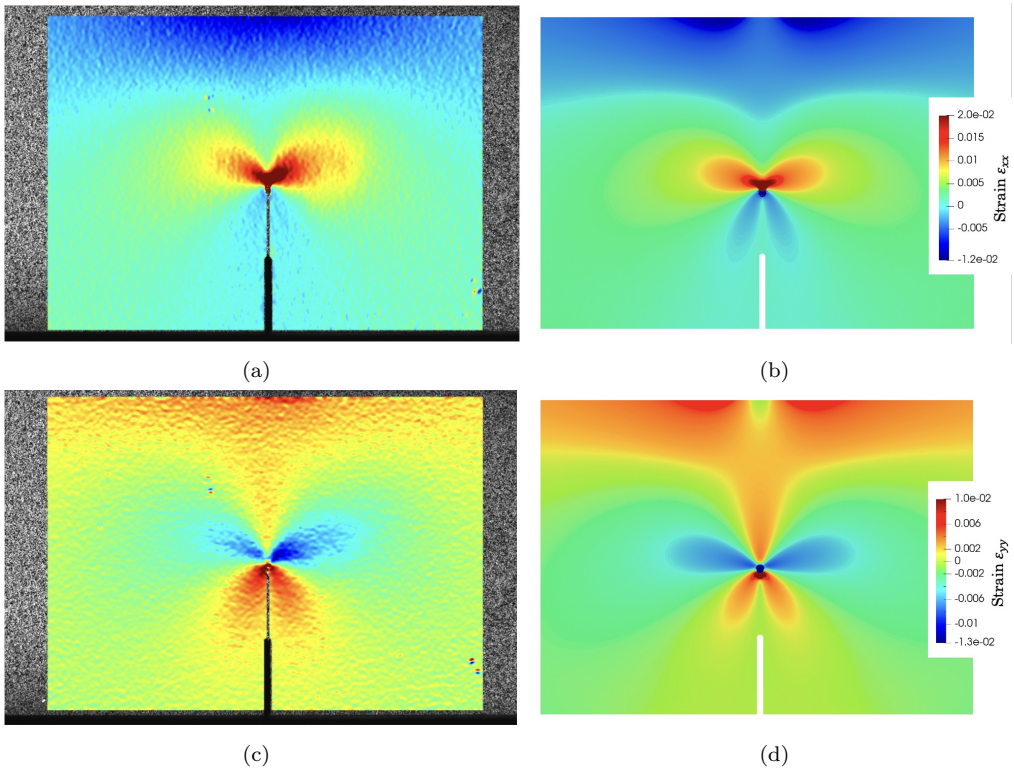

(a) (b)

(c) (d)

Figure 15: Comparison of the experimental (left) and numerical (right) strain fields for W47 SENB pre-cracked samples at a macroscopic compressive displacement of 0.8 mm.

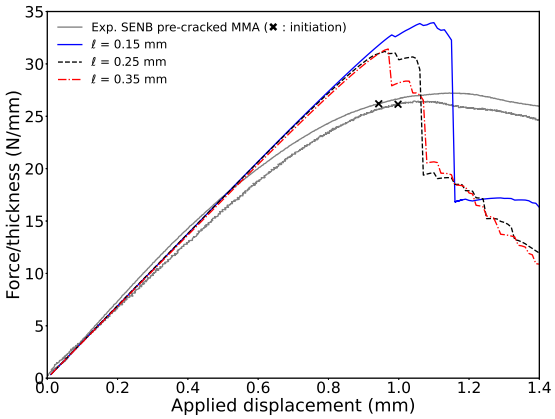

Figure 16: Phase-field modeling of the fracture of W47 pre-cracked samples upon SENB tests.

ℓ, which is in favor of a critical energy release rate in the vicinity of 3.0 kJ/m^2 as provided by the J-integral. Once again, this is confirmed by the plastic dissipation reaching only 2.5% of the total energy only, when the crack initiates, the plasticity being localized at the crack tip only (Figure 17).

Like for the pre-notched samples, we explored the impact of functional $b(d)$ on the crack initiation and propagation. The case of pre-cracked samples is actually more interesting. Like for the pre-notched samples, changing $b(d)$ into $(1-d)$, and even more when setting it to 1, decreases the amount of plasticity developing around the crack tip. However, while decreasing the plastic dissipation is expected to delay the crack initiation, it also keeps the crack sharper favoring an early propagation, as one could notice for the PMMA pre-notched versus pre-cracked samples. In Figure 18, one reads that while approximately the same, the macroscopic applied strain at which the crack initiates, decreases when $b(d)$ evolves from $(1-d)^2$ to $(1-d)$ and 1. The propagation phase confirms the lack of plasticity when $b(d) = 1$, with a smooth continuous propagation, while both cases of $b(d) = (1-d)$ and $b(d) = (1-d)^2$ exhibit similar crack jumps revealed by the force-displacement curves, sign of plasticity at the crack tip.

In the end, very similar results were obtained while modeling the SENB test with pre-notched and pre-cracked samples. The plasticity is very limited and localized at the crack tip, the critical energy release rate values estimated with the J-integral are reliable, the crack propagation is not well reproduced.

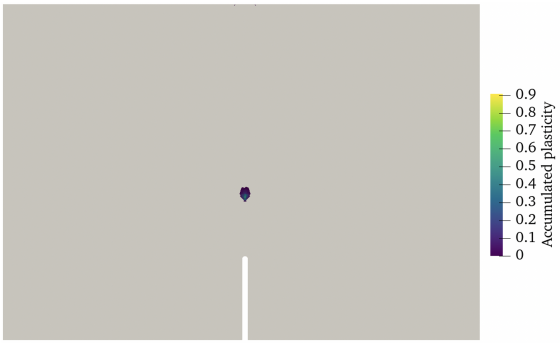

Figure 17: Illustration of accumulated plasticity $\overline{p}$ for W47 pre-cracked sample at an applied macroscopic displacement of 0.8mm. Values under 0.001 (or 0.1 %) are displayed in gray.

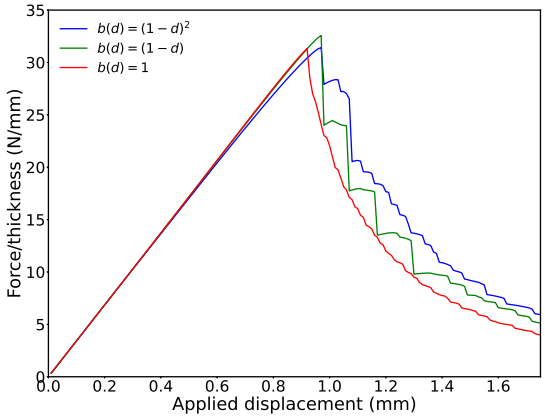

Figure 18: Impact of damage function $b(d)$ penalizing the plastic energy for the pre-cracked sample ($\ell = 0.35$ mm and $G_c = 3$ kJ/m^2).

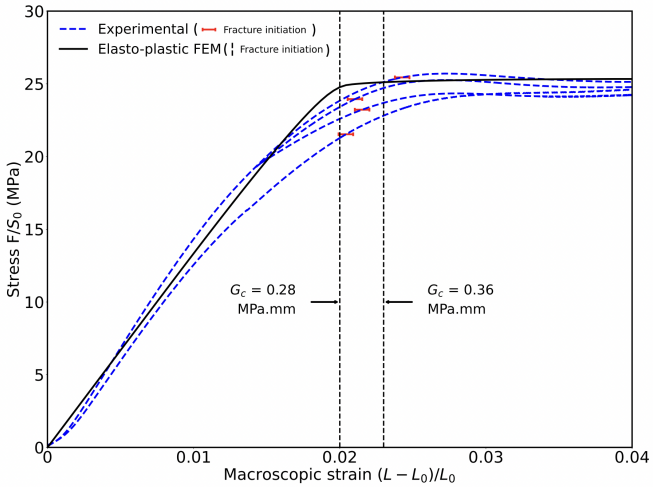

Figure 19: W47 DCDC test - Phase-field model estimates of G_c at initiation compared to experimental results. G_c lower and upper bounds are estimated based on the experimental mean displacement and its standard deviation.

4.3. Fracture toughness for W47 DCDC tests

The DCDC test is simulated within plane stress assumptions. The damage is allowed to evolve only in a vertical band containing the initial notch to avoid undesired damage at the equators of the hole. For details on these simulations, the interested reader is referred to [28]. The inputs include the same material parameters as for the SENB simulations. The parameter ℓ was varied between 0.05 and 0.125 mm without changes into the macroscopic response, the strain and stress at crack initiation, and the crack propagation. As Figure 20 shows, very satisfactory results in terms of macroscopic behavior and strain at initiation were obtained for values of G_c in the range [0.28,0.36] kJ/m^2.

Contrary to the SENB test, the plastic dissipation is not negligible as plasticity develops not only at the crack tip but also in bands starting at the equators of the hole and increasing toward the exterior of the sample at angles of 45° from the vertical axis. The plastic energy represents 20% of the total energy at crack initiation. The significant plasticity occurring before crack initiation seems to explain the negligible impact of parameter ℓ for the DCDC test.

Finally, when considering the case $b(d) = 1$, no plasticity is witnessed at the crack tip and the crack initiation is delayed as shown in Figure 20. For

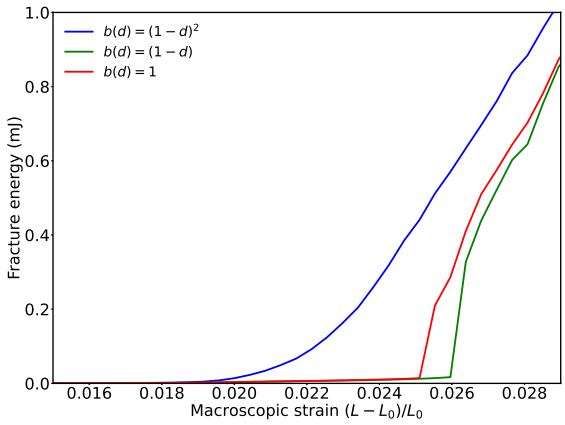

Figure 20: DCDC test fracture energy with respect to the applied macroscopic strain for different functions $b(d)$ in Eq. (3).

the case $b(d) = (1-d)$, some plasticity is witnessed at the crack tip but three time less than when $b(d) = (1-d)^2$, which explains that the crack initiation is also delayed.

4.4. Comparison of the fracture toughness for SENB and DCDC tests

The discrepancy between the values of G_c obtained for the PMMA has been discussed already in section 2.3.2. While the values assessed here are in agreement with the literature for each test, the critical energy release rate estimates vary significantly from the SENB test to the DCDC test.

For material W47, the numerical values of G_c obtained when reproducing the SENB test, confirmed the assumption of confined plasticity and the critical energy release rate values estimated thanks to a simple computation of the J-integral. Moreover, the values that have been measured here are in good agreement with other ones reported in the literature for structural adhesives with similar applications [65, 66]. The values obtained from the SENB tests are significantly higher than the one obtained through DCDC analysis, independently of the type of the initial damage. This result is in accordance with the comparison made on the PMMA. The DCDC test provides with much lower estimate of the critical energy release rate than the SENB test. Despite the fact that, unlike SENB samples, W47 DCDC samples showed significantly plasticity upon loading, the difference in the critical

energy release rate values is difficult to attribute to plasticity since similar difference has been obtained on the PMMA.

Both materials show similar results, the DCDC test predicts significantly lower resistance to crack opening compared to the SENB test, despite the fact that both tests favor mode I opening fracture and that mixed mode fracture seems unlikely to happen for either test. This leaves opened the question: Which test should be carried out to characterize Mode I open fracture of polymers?'.

5. Conclusion

This study has compared the fracture toughness of an elastic and an elasto-plastic polymer through two distinct Mode-I fracture characterization tests, classically carried out, as for DCDC and SENB. The two testing methods had been scarcely compared showing no clear unanimous answer on the similarity of the results they could provide. The results obtained in this study underlined the fracture toughness sensitivity to the chosen test, with DCDC tests yielding significantly lower fracture energy release rate values compared to SENB tests for both materials.

First, considering an elastic PMMA, the LEFM analysis run on both tests concluded in a ratio of four between the SENB test and the DCDC test critical energy release rate values, the DCDC test being more conservative. This result has been obtained while the values of G_c obtained for each test were successfully compared with the literature.

Second, considering an elastoplastic methyl methacrylate polymer, used as structural adhesive, the same experiments were analyzed thanks to finite element simulations implementing the phase-field damage approach. In the case of SENB, limited plasticity was observed, which allowed a simple computation of G_c through the estimate of the J-integral, from the experimental strain field characterization. Values just above and under 3.0 kJ/m^2 for pre-notched and pre-cracked samples respectively, are of the same order of magnitude as other structural adhesives found in the literature. These values were also obtained by finite element analysis, confirming the relevance of the analysis. As for DCDC, the critical energy release rate could be obtained by finite element analysis only, and stand as one order of magnitude lower than for the SENB test.

The divergence between both tests that should characterize the same material parameter, underlines the complexity of material fracture charac-

terization under different loading conditions. It emphasizes the need for further investigation of the experimental fracture tests with advanced modeling techniques to gain deeper insights into the impact of the material behavior and the structure characteristics on the experimental results. This is deeply needed to predict the fracture of polymers in engineering applications that covers 3D heterogeneous loadings.

Acknowledgement

The work is part of the Ph.D. of A. Coq supported by the Chair "Modelling advanced polymers for innovative material solutions" led by Ecole Polytechnique (l'X) and the Fondation de l'Ecole Polytechnique and sponsored by Arkema. The authors thank Ing. Eric Grimbretière for its help on designing and building some of the experimental setups, and student Ridwan Khalidi for running some experiments on the PMMA material. Finally, simulations were run on the Cholesky cluster from Ecole Polytechnique.

Appendix A. *J*-integral calculation

Note that for mode-I fracture in elasto-plastic materials, the path independence of J is not necessarily satisfied. For the SENB samples, the integral J has been calculated along three different paths presented in Figure A.21, decomposing each path in five segments according to their exterior normal $J = \sum_{i=1}^{5} J_i$ with,

$$J_1 = \int_A^B \left(\sigma_{xy}\frac{du}{dx} + \sigma_{yy}\frac{dv}{dx}\right) dx \text{ and } J_3 = \int_B^C \left(\sigma_{xy}\frac{du}{dx} + \sigma_{yy}\frac{dv}{dx}\right) dx$$

$$J_2 = \int_C^D \left(0.5\left(\sigma_{xx}\epsilon_{xx} + \sigma_{yy}\epsilon_{yy} + 2\sigma_{xy}\epsilon_{xy}\right) - \sigma_{xx}\frac{du}{dx} - \sigma_{xy}\frac{dv}{dx}\right) dy$$

$$J_4 = \int_D^E \left(0.5\left(\sigma_{xx}\epsilon_{xx} + \sigma_{yy}\epsilon_{yy} + 2\sigma_{xy}\epsilon_{xy}\right) - \sigma_{xx}\frac{du}{dx} - \sigma_{xy}\frac{dv}{dx}\right) dy$$

$$J_5 = \int_F^A \left(0.5\left(\sigma_{xx}\epsilon_{xx} + \sigma_{yy}\epsilon_{yy} + 2\sigma_{xy}\epsilon_{xy}\right) - \sigma_{xx}\frac{du}{dx} - \sigma_{xy}\frac{dv}{dx}\right) dy$$

with

$$\begin{bmatrix}\sigma_{xx}\\ \sigma_{yy}\\ \sigma_{xy}\end{bmatrix} = \frac{E}{(1-\nu^2)}\begin{bmatrix}1 & \nu & 0\\ \nu & 1 & 0\\ 0 & 0 & \frac{1-\nu}{2}\end{bmatrix}\begin{bmatrix}\epsilon_{xx}\\ \epsilon_{yy}\\ 2\epsilon_{xy}\end{bmatrix} \tag{A.1}$$

the strain field $[\epsilon_{xx}, \epsilon_{yy}, \epsilon_{xy}]$ characterized by digital image correlation and with material parameters $E = 1400$ MPa and $\nu = 0.4$. The results are shown in Figure A.21, proving the path-independence for contours C_2 and C_3. The critical energy release rate G_c has been estimated as the value of J calculated on contour C_3 when the cracks starts to advance.

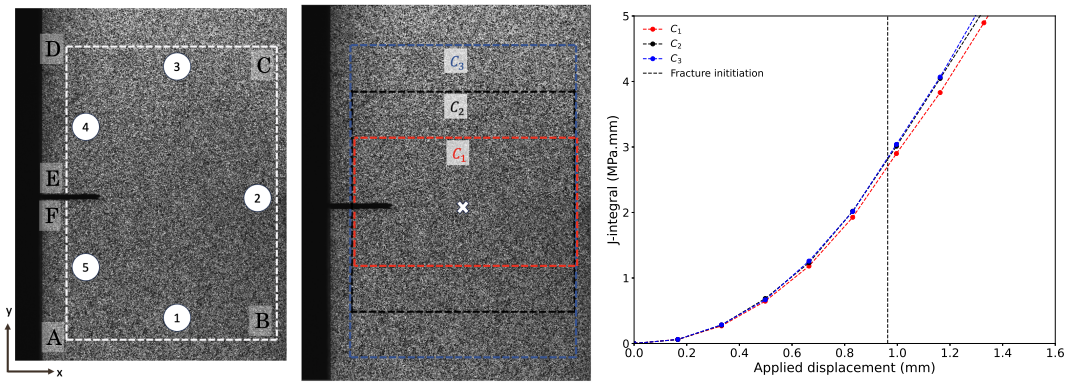

Figure A.21: Computation of the J-integral and validation of the path independence.

Appendix B. Account for Drucker-Prager plasticity criterion

As one can read in Figure 1, material W47 yield stresses in tension (σ_t) and in compression (σ_c) differ. In order to take into account this property, one might apply a Drucker-Prager plasticity criterion that writes as,

$$\sqrt{J_2} = A + B\, tr(\sigma) \tag{B.1}$$

with $J_2 = \frac{1}{2}\left(\underline{\underline{s}} : \underline{\underline{s}}\right)$ and,

$$A = \frac{2}{\sqrt{3}} \frac{\sigma_t\, \sigma_c}{\sigma_c + \sigma_t},\ B = \frac{1}{\sqrt{3}} \frac{\sigma_t - \sigma_c}{\sigma_c + \sigma_t}. \tag{B.2}$$

In our case $\sigma_c = 34$ MPa and $\sigma_t = 20$ MPa.

If one chooses to keep true the normality rule and the no volume change for the plastic strain, the previous total energy expression Eq. (3) remains when replacing σ_y by $\sqrt{3}\,(A + Btr(\sigma))$. Therefore the minimization problem remains the same. Considering $b(d) = 1 - d^2$, and a value of $G_c = 0.34\ \mathrm{kJ/m^2}$, we show in Figures B.22 and B.23, the comparison of the numerical results

for the DCDC test when considering a von Mises material with $\sigma_c = \sigma_t = 34$ and a Drucker-Prager one with $\sigma_c = 34$ MPa and $\sigma_t = 20$ MPa.

Figure B.22 shows similar macroscopic stress-strain response and energy dissipated by plasticity for both cases. However, Figure B.23, displaying the energy dissipated by fracture with respect to the applied strain, presents some interesting features. First, the initiation of the crack propagation occurs at more or less the same macroscopic strain. Therefore, the value of the critical energy release rate G_c predicted by the von Mises model is similar as the one predicted by the Drucker-Prager model. Second, the kinetic of propagation appears slower for the Drucker-Prager model, which is in better agreement with the experiment [28].

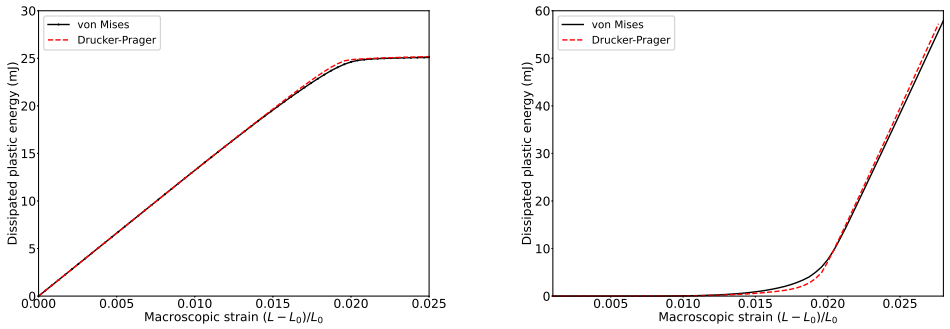

(a) (b)

Figure B.22: Comparison of the DCDC test simulation for a von Mises material and a Drucker-Prager one. (a) Macroscopic stress-strain response (b) Plastic energy dissipated with respect to the applied macroscopic strain.

For the SENB test, the Drucker-Prager model appeared to create some numerical difficulties that have been only partially resolved. It was not possible to consider a Drucker-Prager material with such a spread between σ_c and σ_t. Nonetheless, simulations considering the values $\sigma_c = 34$ MPa and $\sigma_t = 24$ MPa reached convergence and provide an interesting comparison with the calculations run above for a von Mises material with $\sigma_c = \sigma_t = 34$.

Considering, the realistic value of $G_c = 2.86$ kJ/m^2 for both cases, Figure B.24(a) compares the macroscopic stress-strain responses for the pre-cracked SENB sample, showing that fracture happens earlier in terms of strain and at a lower stress for the Drucker-Prager material. The lower stress is favorable when comparison is made with the experimental results. The fact that frac-

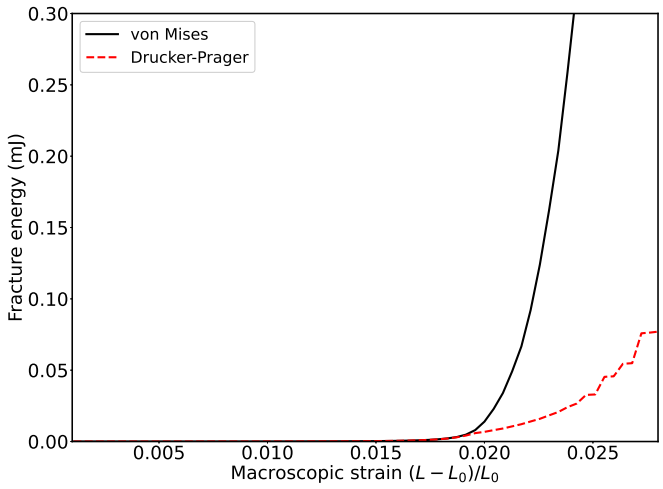

Figure B.23: DCDC test: Comparison of the energy dissipated by fracture as the crack progresses for a material defined by a von Mises or Drucker-Prager plasticity criterion.

ture appears earlier indicates that the von Mises material overestimates the critical energy release rate values but in a relatively moderate range which does not interfere with the general conclusion of the paper, i.e. that the critical energy release rate estimated by the SENB test is significantly higher than the one estimated by the DCDC test. Figure B.24(b) shows logically more plasticity develops for the Drucker-Prager material. However, the amount of energy dissipated by plasticity remains very small compared to the DCDC test (Figure B.22(b)). Finally, Figure B.25 confirms the fact that for the same value of G_c, the crack initiates earlier for the Drucker-Prager material than for the von Mises one.

References

[1] M. L. Dunn, W. Suwito, S. Cunningham, Fracture initiation at sharp notches: Correla tion using critical stress intensities, International Journal of Solids and Structure 34 (1997) 3873–3883. doi:10.1016/S0020-7683(96)00236-3.

[2] M. L. Dunn, W. Suwito, S. Cunningham, C. May, Fracture initiation at sharp notches under mode i, mode ii, and mild mixed

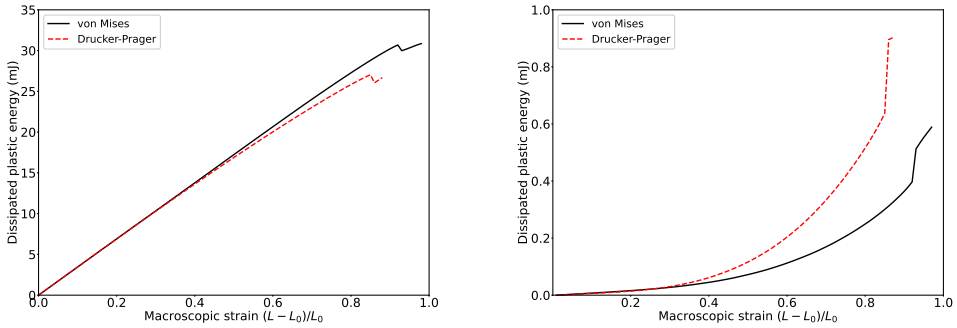

Figure B.24: Comparison of the pre-cracked SENB test simulations for a von Mises material and a Drucker-Prager one. (a) Macroscopic stress-strain response (b) Plastic energy dissipated with respect to the applied macroscopic strain.

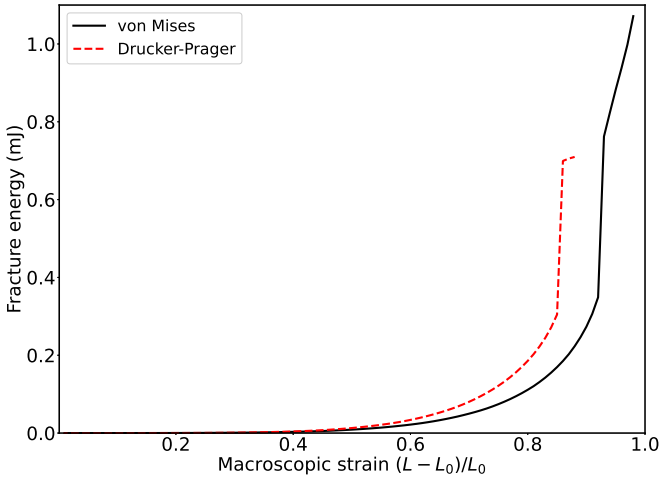

Figure B.25: Pre-cracked SENB test: Comparison of the energy dissipated by fracture as the crack progresses for a material defined by a von Mises or Drucker-Prager plasticity criterion.

mode loading, International Journal of Fracture 84 (1997) 367—381. doi:10.1023/A:1007346203407.

[3] M. Elices, G. Guinea, J. Gómez, J. Planas, The cohesive zone model:

advantages, limitations and challenges, Engineering Fracture Mechanics 69 (2002) 137–163. doi:10.1016/S0013-7944(01)00083-2.

[4] J. Gómez, M. Elices, A fracture criterion for sharp v-notched samples, International Journal of Fracture 123 (2003) 163–175.

[5] J. Yosibah, A. Bussiba, I. Gilad, Failure criteria for brittle elastic materials, International Journal of Fracture 125 (2004) 307–333.

[6] J. Loya, E. Villa, J. Fernández-Sáez, Crack-front propagation during three-point-bending tests of polymethyl-methacrylate beams, Polymer Testing 29 (2010) 113–118. doi:10.1016/j.polymertesting.2009.09.012.

[7] S. Cicero, V. Madrazo, I. Carrascal, Analysis of notch effect in PMMA using the theory of critical distances, Engineering Fracture Mechanics 86 (2012) 56–72.

[8] M. Aliha, A. Bahmani, S. Akhondi, Mixed mode fracture toughness testing of PMMA with different three- point bend type specimens, European Journal of Mechanics A/Solids 58 (2016) 148–162.

[9] M. Ayatollahi, B. Bahramia, A. M. M. Y. Yahya, Effects of support friction on mode i stress intensity factor and fracture T toughness in senb testing, Theoretical and Applied Fracture Mechanics 103 (2019) 102288.

[10] W. Zhou, J. Huang, W. Huang, D. Liu, Dynamic fracture testing of polymethyl-methacrylate (PMMA) single-edge notched beam, Polymer Testing 125 (2020) 307–333. doi:10.1016/j.polymertesting.2020.106833.

[11] J. de Souza, H. N. Yoshimura, F. M. Peres, C. Schön, Effect of sample pre-cracking method and notch geometry in plane strain fracture toughness tests as applied to a pmma resin, Polymer Testing 21 (2012) 834–840. doi:10.1016/j.polymertesting.2012.06.003.

[12] A. Martínez, N. Leon, A. David, J. Rodriguez, A. Salazar, On the effect of the different notching techniques on the fracture toughness of petg, Polymer Testing 32 (2013) 1244–1252. doi:10.1016/j.polymertesting.2013.07.016.

[13] Y. Qiao, M. Salviato, Compression-induced axial crack propagation in DCDC polymer samples: experiments and modeling, Engineering Fracture Mechanics 213 (2019) 110–117. doi:10.1016/j.engfracmech.2019.03.033.

[14] C. Susanti, T. Nakao, H. Yoshihara, Examination of the failure behaviour of wood with a short crack in the tangential–radial system by single-edge-notched bending test, Engineering Fracture Mechanics 77 (2010) 2527–2536. doi:10.1016/j.engfracmech.2010.05.019.

[15] J. Williams, Fracture mechanics of polymers, Polymer and Engineering Science 17 (1977) 3144–149.

[16] M. Dekkers, S. Hobbs, Ductile tearing instability in some engineering thermoplastic blends, Polymer Engineering and Science 27 (1987) 1164–1169.

[17] K. Allaer, I. D. Baere, W. V. Paepegem, J. Degrieck, Direct fracture toughness determination of a ductile epoxy polymer from digital image correlation measurements on a single edge notched bending sample, Polymer Testing 42 (2015) 199–207. doi:10.1016/j.polymertesting.2015.01.014.

[18] X.-K. Zhu, J. Joyce, Review of fracture toughness (G, K, J, CTOD, CTOA) testing and standardization, Engineering Fracture Mechanics 85 (2012) 1–46. doi:10.1016/j.engfracmech.2012.02.001.

[19] J. Rice, A path integral and the approximate analysis of strain concentration by notches and cracks, Journal of Applied Mechanics 35 (1968) 379–386. doi:10.1115/1.3601206.

[20] A. Kojouri, H. Rikaee, K.-A. Kalteremidou, D. V. Hemelrijck, Experimental evaluation of j-integral in elastic and elastic–plastic polymers by means of digital image correlation and higher-order eigenfields under mode-i, Engineering Fracture Mechanics 291 (2023) 109534. doi:10.1016/j.engfracmech.2023.109534.

[21] S. Choi, J. Salem, Fracture toughness of pmma as measured with indentation cracks, Journal of Material Research 8 (1993) 3210–3217.

[22] M. Ayatollahi, M. R. Moghaddam, N. Razavia, F. Berto, Geometry effects on fracture trajectory of pmma samples under pure mode-i loading, Engineering Fracture Mechanics 163 (2016) 449–461.

[23] J. Triclot, T. Corre, A. Gravouil, V. Lazarus, Key role of boundary conditions for the 2d modeling of propagation in linear elastic compact tension tests, Engineering Fracture Mechanics 277 (2023) 109012. doi:10.1016/j.engfracmech.2022.109012.

[24] C. G. Sammis, The failure of brittle porous solids under compressive stress states, Acta Metallurgica Materialia 34 (1986) 511–526.

[25] T. Plaisted, A. Amirkhizi, S. Nemat-Nasser, Compression-induced axial crack propagation in DCDC polymer samples: experiments and modeling, International Journal of Fracture 141 (2006) 447–457. doi:10.1007/s10704-006-9006-9.

[26] C. Nielsen, A. V. Amirkhizi, S. Nemat-Nasser, The effect of geometry on fracture strength measurement using DCDC samples, Engineering Fracture Mechanics 91 (2012) 1–13. doi:10.1016/j.engfracmech.2012.04.030.

[27] M. George, Y. Nziakou, S. Goerke, A.-C. Genix, B. Bresson, S. Roux, H. Delacroix, M. C. J.-L. Halary and, In situ afm investigation of slow crack propagation mechanisms in a glassy polymer, Journal of the Mechanics and Physics of Solids 112 (2018) 109–125.

[28] A. Coq, J. Diani, S. Brach, Comparison of the phase-field approach and cohesive element modeling to analyze the double cleavage drilled compression fracture test of an elastoplastic material, International Journal of Fracture (2024).

[29] Y. Nziakou, Analyse multi-échelle des mécanismes d'endommagement des matériaux composites amorphologie complexe destinés à l'aéronautique, Ph.D. thesis, Université Pierre et Marie Curie (2015).

[30] K. Idonije, M. Motuku, d. I. S. a, H. Aglan, Evaluation of the stress intensity factor of brittle polymers based on the crack arrest concept, Journal of Reinforced Plastics and Composites 12 (1993) 778–786.

[31] G. A. Francfort, J.-J. Marigo, Revisiting brittle fracture as an energy minimization problem, Journal of the Mechanics and Physics of Solids 46 (1998) 1319–1342.

[32] J. Blaber, B. Adair, A. Antoniou, Ncorr: Open-source 2d digital image correlation matlab software, Experimental Mechanics 55 (6) (2015) 1105 – 1122. doi:10.1007/s11340-015-0009-1.

[33] H. Remesan, M. Ramji, Adaptation of open source 2d dic software ncorr for solid mechanics applications, 2014. doi:10.13140/2.1.4994.1442.

[34] Standard test methods for plane-strain fracture toughness and strain energy release rate of plastic materials, Standard, ASTM International, West Conshohocken (2014).

[35] G. Irwin, J. Kies, Fracturing and fracture dynamics, Welding Journal 31 (2) (1952) 95–100.

[36] J. J. Benbow, F. C. Roesler, Proc. Phys. Soc. 70B (201) (1956).

[37] N. L. Svensson, Proc. Phys. Soc. 77 (1961).

[38] J. Berry, Determination of fracture surface energies by the cleavage technique, Journal of Applied Physics 34 (1) (1963) 62–68. doi:10.1063/1.1729091.

[39] L. Hao, H. Yu, Z. Shen, S. Zhu, B. Wang, C. Huang, L. Guo, Determination of mode-ii critical energy release rate using mixed-mode phase-field model, Theoretical and Applied Fracture Mechanics 125 (2023) 103840. doi:10.1016/j.tafmec.2023.103840.

[40] A. Salazar, Y. Patel, J. Williams, Influence of crack sharpness on the fracture toughness of epoxy resins, 13th International Conference on Fracture, 2013.

[41] S. Cicero, V. Madrazo, I. Carrascal, R. Cicero, Assessment of notched structural components using failure assessment diagrams and the theory of critical distances, Engineering Fracture Mechanics 78 (2011) 2809–2825. doi:10.1016/j.engfracmech.2011.08.009.

[42] Y. Qiao, M. Salviato, Strength and cohesive behavior of thermoset polymers at the microscale: A size-effect study, Engineering Fracture Mechanics 213 (2019) 100–117. doi:10.1016/j.engfracmech.2019.03.033.

[43] M. Braun, J. Aranda-Ruiz, J. Fernández-Sáez, Mixed mode crack propagation in polymers using a discrete lattice method. (2021). doi:10.3390/polym13081290.

[44] G. Catalanotti, P. Camanho, J. Xavier, C. Dávila, A. Marques, Measurement of resistance curves in the longitudinal failure of composites using digital image correlation, Composites Science and Technology 70 (13) (2010) 1986–1993, iCCM-17: Composites In Biomedical Applications. doi:10.1016/j.compscitech.2010.07.022.

[45] M. A. Bouaziz, J. Marae-Djouda, Z. Marouene, J. Gardan, F. Hild, Crack growth measurement and j-integral evaluation of additively manufactured polymer using digital image correlation and fe modeling, Fatigue and Fracture of Engineering Materials and Structures (2021) 1–18doi:10.1111/ffe.13431.

[46] T. Michalske, W. Smith, E. Chenr, Stress intensity calibration for the double cleavage drilled compression specimen, Engineering Fracture Mechanics 45 (1993) 637–642.

[47] M. He, M. Turner, A. Evans, Analysis of the double cleavage drilled compression specimen for interface fracture energy measurements over a range of mode mixities, Acta Metallurgica Materialia 84 (1995) 104070.

[48] T. Fett, G. Rizzi, D. Munz, T-stress solution for DCDC specimens, Engineering Fracture Mechanics 72 (2005) 145–149.

[49] G. Pallares, L. Ponson, A. Grimaldi, M. George, G. Prevot, M. Ciccotti, Crack opening profile in DCDC specimen, International Journal of Fracture 156 (2009) 11–20. doi:10.1007/s10704-009-9341-8.

[50] Q. Wang, M. Ni, L. Wu, R. Huang, Scrutinized and revised stress intensity factor formulas for double cleavage drilled compression specimens, Theoretical and Applied Fracture Mechanics 96 (2018) 803–810.

[51] L. J. Broutman, F. J. McGarry, Fracture surface work measurements on glassy polymers by a cleavage technique. i. effects of temperature, Journal of Applied Polymer Science 9 (2) (1965) 589–608. doi:10.1002/app.1965.070090221.

[52] B. Bourdin, G. A. Francfort, J.-J. Marigo, Numerical experiments in revisited brittle fracture, Journal of the Mechanics and Physics of Solids 48 (2000) 797–826.

[53] E. Tanné, T. Li, B. Bourdin, J. Marigo, C. Maurini, Crack nucleation in variational phase-field models of brittle fracture, Journal of Mechanics and Physics of Solids 10 (2018) 80–99.

[54] S. Brach, E. Tanné, B. Bourdin, K. Bhattacharya, Phase-field study of crack nucleation and propagation in elastic–perfectly plastic bodies, Computer Methods in Applied Mechanics and Engineering 353 (2019) 44–65.

[55] S. V. Roberto Alessi, Jean-Jacques Marigo, Gradient damage models coupled with plasticity and nucleation of cohesive cracks, Archive for Rational Mechanics and Analysis 214 (2) (2014) 575–615.

[56] R. Alessi, M. Ambati, T. Gerasimov, S. Vidoli, L. D. Lorenzis, Comparison of phase-field models of fracture coupled with plasticity, Advances in Computational Plasticity 46 (2018) 1–21.

[57] A. Fischer, J.-J. Marigo, Gradient damage models coupled with plasticity and their application to dynamic fragmentation, 2019.

[58] M. Ambati, T. Gerasimov, L. Lorenzis, Phase-field modeling of ductile fracture, Computational Mechanics 55 (2015) 1017–1040.

[59] C. Miehe, M. Hofacker, L.-M. Schänzel, F. Aldakheel, Phase field modeling of fracture in multi-physics problems. part ii. coupled brittle-to-ductile failure criteria and crack propagation in thermo-elastic–plastic solids, Computer Methods in Applied Mechanics and Engineering 294 (2015) 486–522. doi:10.1016/j.cma.2014.11.017.

[60] K. Pham, H. Amor, J.-J. Marigo, C. Maurini, Gradient damage models and their use to approximate brittle fracture, International Journal of Damage Mechanics 20 (2010) 618–652. doi:10.1177/1056789510386852.

[61] R. Alessi, J.-J. Marigo, C. Maurini, S. Vidoli, Coupling damage and plasticity for a phase-field regularisation of brittle, cohesive and ductile fracture: One-dimensional examples, International Journal of Mechanical Sciences 149 (2018) 559–576. doi:10.1016/j.ijmecsci.2017.05.047.

[62] A. Logg, K.-A. Mardal, G. N. Wells (Eds.), Automated Solution of Differential Equations by the Finite Element Method, Springer, 2012.

[63] C. Geuzaine, J.-F. Remacle, Gmsh: a three-dimensional finite element mesh generator with built-in pre- and post-processing facilities, International Journal for Numerical Methods in Engineering 79 (2009) 1309–1331.

[64] E. Tanne, Variational phase-field models from brittle to ductile fracture : nucleation and propagation, Ph.D. thesis (12 2017).

[65] Y. Hua, A. R. M. Kasavajhala, L. Gu, Elastic–plastic analysis and strength evaluation of adhesive joints in wind turbine blades, Composites Part B: Engineering 44 (1) (2013) 650–656. doi:10.1016/j.compositesb.2012.02.001.

[66] M. A. Eder, R. Bitsche, Fracture analysis of adhesive joints in wind turbine blades, Wind Energy (2015). doi:10.1002/we.1744.